**Title:** Super-resolution microscopy of the ß-carboxysome reveals a homogenous matrix

**Authors:** Matthew J. Niederhuber *,†, Talley J. Lambert‡, Clarence Yapp§, Pamela A. Silver*,†, Jessica K. Polka*,†

**Affiliations:**

* Department of Systems Biology, Harvard Medical School, 02115, Boston, Massachusetts, United States.

† Wyss Institute for Biologically Inspired Engineering, Harvard University, 02115, Boston, Massachusetts, United States.

‡. Department of Cell Biology, Harvard Medical School, 02115, Boston, Massachusetts, United States.

§. Image and Data Analysis Core, Harvard Medical School, 02115, Boston, Massachusetts, United States.

**Abstract:**

Carbon fixation in cyanobacteria makes a major contribution to the global carbon cycle. The cyanobacterial carboxysome is a proteinaceous microcompartment that protects and concentrates the carbon-fixing enzyme RuBisCO in a paracrystalline lattice, making it possible for these organisms to fix $CO_2$ from the atmosphere. The protein responsible for the organization of this lattice in beta-type carboxysomes of the freshwater cyanobacterium *Synechococcus elongatus*, CcmM, occurs in two isoforms thought to localize differentially within the carboxysome matrix. Here, we use widefield timelapse and 3D-structured illumination microscopy (3D-SIM) to study the recruitment and localization of these two isoforms. We demonstrate that this super-resolution

technique is capable of successfully resolving the outer protein shell of the carboxysome from its internal cargo. We develop an automated analysis pipeline to analyze and quantify 3D-SIM images and generate a population level description of carboxysome shell protein, RuBisCO, and CcmM isoform localization. We find that both CcmM isoforms colocalize in space and time, prompting a revised model of the internal arrangement of the beta carboxysome.

**Introduction:**

RuBisCO (ribulose-1,5-bisphosphate carboxylase/oxygenase), the primary enzyme of carbon fixation, is ubiquitous in autotrophic organisms. However, it is notoriously inefficient and readily participates in energetically wasteful side-reactions with $O_2$ (Andersson *et al*., 2008). Many organisms that rely on RuBisCO to acquire inorganic carbon tune the enzyme's local microenvironment to achieve sufficient levels of carbon fixation. While plants can do this within membrane barriers, many single-celled organisms have evolved a strategy of proteinaceous compartmentalization.

The carboxysome is a bacterial microcompartment (BMC) found in cyanobacteria and prokaryotic chemoautotrophs. Composed of thousands of individual subunits, the carboxysome encapsulates RuBisCO and carbonic anhydrase (CA) within a selectively permeable icosahedral shell, making survival possible at atmospheric levels of $CO_2$ (Figure 1A) (Rae *et al*., 2013; Kerfeld *et al*., 2016).

While evolutionarily distinct carboxysomes share many similar structural features, the RuBisCO in the beta-type carboxysome (ß-carboxysome) of the freshwater cyanobacterium *Synechococcus elongatus* PCC7942 is organized into a paracrystalline lattice (Kaneko *et al*., 2006). The structural protein CcmM has been implicated in connecting individual RuBisCO enzymes into an ordered matrix, resulting in the observed dense crystalline packing (Long *et al*., 2007; Cot *et al*., 2008, Long *et al.,* 2010;

Cameron *et al*., 2013). The full-length 58kDa CcmM protein of PCC7942 is characterized by an N-terminal carbonic anhydrase (CA) binding domain and three repeating domains toward the C-terminal end that have sequence homology to the small subunit of RuBisCO (Figure 1B) (Price *et al*., 1993). Due to an internal ribosomal entry site (IRES), CcmM is translated as two isoforms, a full-length protein (M58) and a 35kDa truncated version (M35) that consists of only the three small subunit like (SSU-like) domains (Long *et al*., 2007; Long *et al*., 2010).

The current model of ß-carboxysome internal structure suggests that the small subunit like domains (SSU-like) of CcmM displace some of the small subunits of the $L_8S_8$ RuBisCO holoenzyme and tether multiple enzymes together into a dense network (Figure 1C) (Long *et al*., 2007; Long *et al*., 2010; Rae *et al*., 2013; Kerfeld *et al.,* 2016). Co-purification and yeast 2-hybrid experiments have shown that RuBisCO readily complexes with both isoforms of CcmM in PCC7942 (Long *et al*., 2007; Cot *et al*., 2008). In addition, fluorescence tagging experiments have demonstrated that M35 alone is capable of nucleating assembly of tagged RuBisCO if at least two of the SSU-like domains are present. However, M35 is not sufficient to cause encapsulation by recruiting shell components in the absence of M58 (Cameron *et al*., 2013). Densitometry analyses of western blot experiments have found imbalanced ratios of RbcS to RbcL (~5:8) in PCC7942 cell lysates, suggesting that the missing RbcS slots may be occupied by CcmM SSU domains (Long *et al*., 2011). These findings have supported a model of carboxysome architecture and step-wise assembly in which M35 nucleates a core of RuBisCO. In this model, M58 is limited to a layer beneath the shell where it can interact with CcmN, CA, and shell components. While this model predicts that the CcmM isoforms are differentially localized and that the timing of their integration may differ, these predictions have yet to be directly tested.

In order to test this model, we fluorescently tagged CcmM to visualize its assembly and the localization of CcmM isoforms *in vivo*. Previous work has shown that completely replacing CcmM with tagged fusions does not disrupt carboxysome function (Long *et al*., 2007; Cameron *et al*., 2015). Loss of either isoform of CcmM creates mutants that fail to produce carboxysomes and have a high $CO_2$ requirement (HCR) for growth (Woodger *et al.,* 2005; Long *et al*., 2010). However, complementation of such mutants with tagged copies of CcmM has been shown to rescue this phenotype (Long *et al*., 2007; Cameron *et al*., 2015).

Here we show the successful complementation of a Δ*ccmM* mutant with a dually fluorescently tagged integration of *ccmM*. This dual tagging strategy does not significantly impair carboxysome formation, morphology, or function. In our timelapse fluorescence microscopy data we find no evidence of differential CcmM isoform assembly during carboxysome biogenesis. Using super-resolution 3D Structured Illumination Microscopy (3D-SIM), we examined the relative localization of carboxysome shell, CcmM, and RuBisCO proteins. Our 3D-SIM data does not support a model of carboxysome internal organization in which M58 is limited to a layer just beneath the external protein shell. These data support a revised model of carboxysome internal structure in which M35 and M58 isoforms are both integrated deep within the core of the carboxysome and are both involved with the early steps of carboxysome assembly.

## Results:

### Fluorescent fusions to CcmM complement a deletion of the wildtype

We integrated an N- and C-terminal fluorescently-tagged copy of *ccmM* (*mTagBFP2-ccmM-mNeonGreen*) driven by the IPTG inducible promoter P*trc* into the genome of an

*S. elongatus* PCC7942 Δ*ccmM*::*HygR* mutant strain (Figure 2A-B) and verified expression with western blot analysis (Figure 2C). This strategy allowed us to visually separate full length CcmM from truncated M35 by blue fluorescence. We found that P*trc* was sufficiently leaky to produce protein without induction. Consequently we never induced the Δ*ccmM* + *mTagBFP2-CcmM-mNeonGreen* strain, including for western blot analysis, unless otherwise noted. We blotted lysates of WT, Δ*ccmM*, and Δ*ccmM* + *mTagBFP2-CcmM-mNeonGreen* strains for the presence of CcmM (Figure 2C). In WT 7942 cells, we detected two bands at ~60 kDa and ~40 kDa, corresponding to the two native CcmM isoforms M58 and M35. In the Δ*ccmM* strain, these bands are absent. In the Δ*ccmM* + *mTagBFP2-CcmM-mNeonGreen* gene complement, we detected two bands at ~140 kDa and ~70 kDa, corresponding to molecular weight shifts of 60kDa (both fluorescent tags) and 30kDa (mNeonGreen alone), respectively. The observed weight shift of the tagged CcmM demonstrates that the CcmM IRES is not impaired by the presence of N- and C-terminal tags, and that both long and short CcmM isoforms are translated. We also made a reciprocally tagged version of the CcmM complement (mNeonGreen-CcmM-mTagBFP2), but did not use it for further analysis because western blotting showed the presence of protein degradation (Supplemental Figure S1).

Our tagged *ccmM* complement grew at a rate comparable to WT at atmospheric levels of $CO_2$ (Figure 2D). We grew WT 7942, the Δ*ccmM* mutant, and the Δ*ccmM* + *mTagBFP2-CcmM-mNeonGreen* complement in ambient air and 2% $CO_2$ conditions, measured optical density at 750nm ($OD_{750}$), and calculated doubling times between the 18- and 90-hour time points. Both WT and Δ*ccmM* cells cultured with 2% $CO_2$ grew well with similar doubling times of 17.6 $\pm$ 0.4 hours ($n$ = 5, Error = SD) and 15.8 $\pm$ 2.1 hours ($n$ = 6, Error = SD) respectively. As expected, Δ*ccmM* mutant growth was dependent on supplemented $CO_2$ (Long *et al*., 2010); these cells showed no growth in ambient air conditions. In contrast, the Δ*ccmM* + *mTagBFP2-CcmM-mNeonGreen* complement grew

130 well in air with a doubling time of 23.3 ± 2.4 hours (*n* = 6, Error = SD). This growth rate is
131 similar to that of WT cells in air, which had a doubling time of 20.6 ± 1.8 hours (*n* = 6,
132 Error = SD), indicating that our engineered strain is capable of fixing carbon, and that
133 carboxysome function is not severely impaired by the dual-fusion *ccmM* complement.
134 Because both the M58 and M35 isoforms of CcmM are required for growth without $CO_2$
135 supplementation (Long *et al*., 2010), our data indicate that both isoforms produced by
136 our dual fusion are functional.

137 Carboxysomes formed in the Δ*ccmM* + *mTagBFP2-CcmM-mNeonGreen*
138 complement were structurally similar to those of WT cells. Using transmission electron
139 microscopy, we imaged ultrathin sections of fixed cells from WT 7942, Δ*ccmM*, and
140 Δ*ccmM* + *mTagBFP2-CcmM-mNeonGreen* strains (Figure 3). Carboxysomes in WT
141 PCC7942 cells had an average maximum width of 179 ± 33 nm (*n* = 26, Error = SD).
142 Carboxysomes in Δ*ccmM* + *mTagBFP2-CcmM-mNeonGreen* cells generally had a
143 normal appearance and shape with visibly angled facets and often clear hexagonal
144 geometry, but were noticeably larger, with an average maximum diameter of 319 ± 92
145 nm (*n* = 41, Error = SD). This is not unexpected; it has been previously reported that His-
146 tagged *ccmM* complements increase carboxysome size (Long *et al.,* 2007).
147 Occasionally, dense masses at the cell poles were observed in Δ*ccmM* + *mTagBFP2-*
148 *CcmM-mNeonGreen* micrographs, most likely indicating protein aggregation. Because
149 we are using this strain without induction and no effective repressors exist, we cannot
150 know if reducing expression would prevent aggregate formation. However, IPTG-
151 induced cells observed with 3D-SIM display a dramatic increase in polar protein
152 aggregation, often filling a large portion of the cell, confirming that overexpression of this
153 construct leads to aggregation (Supplemental Figure S2).
154

155 **Both CcmM isoforms share similar recruitment kinetics and localization**

156 Both CcmM isoforms are recruited to growing carboxysomes with similar timing
157 and kinetics. Using widefield microscopy, we imaged the CcmM complement
158 (mTagBFP2-CcmM-mNeonGreen) at 10 minute intervals for 40 hours (Figure 4). Particle
159 tracking revealed that both the CcmM isoforms assembled slowly, with an average
160 assembly time of approximately 10.50 $\pm$ 5.39 hours ($n$ = 8, Error = SD) for M58-
161 mNeonGreen and M35-mNeonGreen, and 12.06 $\pm$ 7.27 hours ($n$ = 8, Error = SD) for
162 mTagBFP2-M58 (Figure 4C). This is longer than the ~6-7 hour maturation time
163 previously reported for RuBisCO (Chen *et al*., 2013), perhaps as a result of temperature
164 or light levels during imaging. Assembly times were estimated based on the time it took
165 a particle to go from the intensity required for automatic particle detection (methods) to
166 the first value $\geq$ 0.8 on the normalized intensity plot.

167 Next, a four-parameter logistic equation was used to approximately model the
168 particle tracks. These models highlight similar assembly kinetics for both CcmM isoforms
169 within the same carboxysome. Based on these fit curves, half-max values of green and
170 blue particle assemblies were found to have an absolute average difference of 1.18 $\pm$
171 0.68 hours ($n$ = 8, Error = SD). If one CcmM isoform precedes the other during
172 carboxysome biogenesis, the half-max values of each isoform would be expected to be
173 significantly different. However, a comparison of half-max values from eight measured
174 assemblies found no significant difference (Wilcoxon matched-pairs signed rank test,
175 number of pairs = 8, P = 0.945). In order to test if CcmM isoforms differ in rate of
176 assembly, channel specific assembly times (average reported above) were analyzed
177 and found not to be significantly different among paired fluorescent channels (Wilcoxon
178 matched-pairs signed rank test, number of pairs = 8, P = 0.375). This indicates that
179 CcmM isoforms M35 and M58 assembled at relatively similar rates.

180

181 **M58 is not confined to a sub-shell layer in the carboxysome**

182 Super-resolution microscopy of fluorescently tagged M58 and M35 show
183 indistinguishable distributions in the carboxysome. We used 3D-Structured Illumination
184 Microscopy (3D-SIM) to acquire super-resolution images of the Δ*ccmM* + *mTagBFP2-*
185 *CcmM-mNeonGreen* strain, as well as fluorescently tagged RuBisCO (RbcL-sfGFP) and
186 the shell protein CcmK4 (CcmK4-mTagBFP2 and CcmK4-sfGFP) in PCC7942. 3D-SIM
187 images of strains with both GFP- and BFP-tagged CcmK4 resolved the external
188 carboxysome shell as a ring structure in the xy-plane (Figure 5A-F), demonstrating that
189 3D-SIM provides sufficient resolution to identify peripherally localized proteins in the
190 carboxysome. To confirm these rings were not an artifact of SIM reconstruction, we
191 imaged a strain of PCC7942 integrated with a GFP labeled copy of the large subunit of
192 RuBisCO (RbcL-sfGFP). This strain has been previously used successfully to study
193 RuBisCO assembly and spacing (Savage *et al*., 2010; Chen *et al*., 2013). 3D-SIM of
194 RbcL-sfGFP showed no ring-like structures, producing only solid regularly-spaced
195 particles (Figure 5G-I). To test if M58 was in fact limited to a sub-shell layer, we imaged
196 the Δ*ccmM* + *mTagBFP2-CcmM-mNeonGreen* gene complement with 3D-SIM. Both
197 CcmM isoforms produced solid objects similar to those observed with the RbcL-sfGFP
198 strain (Figure 5J-N). These qualitative results suggested that the tagged M58 isoform of
199 CcmM was not excluded from integration into the carboxysome core as would be
200 expected if the protein was only present as a thin layer just beneath the exterior shell.
201 The reconstructed intensity histogram (RIH) score from the SIMcheck plugin (Ball *et al*.,
202 2015) was used to verify reconstruction quality. Reconstruction scores for all conditions
203 were of similar quality (Supplemental Table S1).

204 We developed an automated image analysis pipeline and a metric to quantify the
205 degree to which fluorescently-labeled proteins were localized at the perimeter of the
206 carboxysome versus uniformly distributed throughout the matrix. The max-to-center

intensity (MTC) ratio is calculated for each particle as the peak intensity of the average radial profile divided by the intensity at the particle centroid. A perfectly uniform protein distribution would result in the peak particle intensity overlapping the particle centroid, and yield an MTC ratio of 1.00. Higher MTC values result from particles with decreased intensity at their centers, indicating a more ring-link appearance.

ANOVA testing confirmed that mean MTC values were significantly heterogeneous between all the labeled carboxysome proteins (Welch's ANOVA, $F_{4, 7378}$=160.48, $P$<0.001). A Games-Howell test with $q_{critical}$(k=5, df=∞, α=0.001)=5.484 was then used to make further pairwise comparisons of labeled carboxysome protein MTC values (Supplementary Table S2). This automated analysis of RbcL-sfGFP and CcmK4-sfGFP images confirmed our initial observations that carboxysomes appear fundamentally different between these strains (Games-Howell test, MD=0.02, $q$=22.26); similar results were obtained from the comparison of RbcL-sfGFP and CcmK4-mTagBFP2 (Games-Howell test, MD=0.03, $q$=26.38) (Figure 6A). RbcL-sfGFP particles had an average diameter of 244 ± 45 nm and an average MTC value of 1.002 ± 0.005 ($n$ = 3505), with a maximum intensity ratio of 1.04. Based on this, we calculated an upper ratio threshold of 1.05, below which objects are likely to be uniform, by adding two standard deviations to the RbcL-sfGFP max ratio of 1.04. This threshold is denoted on MTC ratio versus diameter plots as a horizontal dotted line (Figure 6).

In contrast to RbcL, we found that shell proteins displayed high MTC ratios. CcmK4-sfGFP particles had an average diameter of 253 ± 34 nm ($n$ = 3459), and in comparison to RbcL-sfGFP particles, a significantly greater average MTC ratio of 1.023 ± 0.077 (Games-Howell test, MD=0.02, $q$=22.26) (Figure 6H). Approximately 10% of CcmK4-sfGFP particles have MTC ratios ≥ 1.05, denoting a ring-like appearance (Figure 6B). Analysis of CcmK4-mTagBFP2 particles also revealed a significantly different mean MTC ratio compared to labeled RbcL-sfGFP (Games-Howell test, MD=0.03, $q$=26.38)

233 (Figure 6H), with the CcmK4-mTagBFP2 particles having an average size of 244 ± 32
234 nm and average MTC ratio of 1.036 ± 0.093 (Figure 6C). Of note, the percent of ring-like
235 particles identified in CcmK4-mTagBFP2 cells (18.16% ≥ $MTC_{1.05}$) was significantly
236 greater than the percentage found in CcmK4-sfGFP cells (9.90% ≥ $MTC_{1.05}$) (Games-
237 Howell test, MD=0.01, *q*=8.51) (Figure 6H). This increase in the fraction of rings
238 identified with BFP labeled CcmK4 over those identified with GFP may be the result of
239 the improvement in resolution due to the shorter wavelength of blue versus green
240 fluorophores. Based on the smallest resolvable shell in the CcmK4-mTagBFP2 strain,
241 which had an apparent diameter of 197nm, and accounting for an expected shell depth
242 of 5-6nm, we do not expect to resolve by SIM even true ring-like particles smaller than
243 approximately 220nm in diameter (Kaneko *et al*., 2006). This lower resolvable limit is
244 denoted on plots of tagged M58 and of M35 particles by a grey region in Figure 6D-E.
245 Analysis of the Δ*ccmM* + *mTagBFP2-CcmM-mNeonGreen* gene complement
246 identified a small number of tagged M58 particles as ring-like (Figure 6D). Our analysis
247 found 0.58% (19 of 3303) of the mTagBFP2-M58 particles had MTC ratios of ≥ 1.05,
248 with an average size of 233 ± 46 nm and average MTC ratio of 1.003 ± 0.010 (Figure
249 6F). We found a significant difference in the MTC ratios of mTagBFP2-M58 particles vs
250 both shell-labeled CcmK4-mTagBFP2 (Games-Howell test, MD=0.03, *q*=25.27) and
251 CcmK4-sfGFP (Games-Howell test, MD=0.02, *q*=20.69) (Figure 6H). This supports
252 qualitative observations that particles of the labeled M58 strain did not appear as ring-
253 like as those in the strains with labeled carboxysome shells. mTagBFP2-M58 particles
254 also had significantly different MTC ratios compared to RbcL-sfGFP particles (Games-
255 Howell test, MD=0.001, *q*=10.05), but this difference was produced by only 19 ring-like
256 particles in the mTagBFP2-M58 strain (Figure 6H). Taken together, these test results
257 indicate that though mTagBFP2-M58 labeled carboxysomes have a small but statistically
258 significant number of MTC ratios ≥ 1.05, the mean ratio is not similar to that produced by

259 labeled carboxysome shell proteins, as would have been expected if the M58 isoform
260 followed a strict sub-shell localization.
261 The Δ*ccmM* + *mTagBFP2-CcmM-mNeonGreen* complement, which expresses
262 both full-length M58-mNeonGreen and the short isoform M35-mNeonGreen, produced 2
263 particles with MTC ratios ≥ 1.05 (Figure 6E). Only 0.06% of particles were found above
264 that threshold, with an average size of 244 ± 47 nm ($n$ = 3437) and average MTC ratio of
265 1.002 ± 0.005 (Figure 6F). The mean MTC ratio of these particles was significantly
266 different than those of both labeled CcmK4-sfGFP (Games-Howell test, MD=0.02,
267 $q$=22.20) and CcmK4-mTagBFP2 (Games-Howell test, MD=0.03, $q$=26.34) (Figure 6H).
268 Pair-wise comparison of M58-mNeonGreen and M35-mNeonGreen particles to RbcL-
269 sfGFP found no significant difference in mean MTC ratios (Games-Howell test,
270 MD=0.00005, $q$=0.57) (Figure 6G), indicating that the population of green fluorescent
271 particles produced in the Δ*ccmM* + mTagBFP2-CcmM-mNeonGreen strain were solid,
272 similar to those observed in the strain with labeled RuBisCO.
273
274 **Discussion:**
275 **The carboxysome can support the addition of large foreign proteins via direct**
276 **fusion to CcmM**
277 The function of CcmM and other components of the carboxysome are robust to
278 the addition of large protein fusions, further supporting these fusions as a means to
279 localize foreign cargo to the carboxysome for engineering applications. Previous work
280 has shown that tagged CcmM gene complements can rescue the HCR phenotype of
281 CcmM mutants without significant impairment of carboxysome function compared to WT
282 cells (Long *et al*., 2010; Cameron *et al*., 2015). We find that such complementation is
283 also possible when fluorescent tags are fused to both ends of CcmM, significantly
284 increasing the size of both the M58 and M35 isoforms. These results suggest that

285 heterologous proteins could be simultaneously fused to multiple loci in the matrix,
286 opening the door for localizing multipart enzymatic pathways inside the carboxysome.
287
288 **M35 and M58 assemble simultaneously during carboxysome biogenesis**
289 M35 has been hypothesized to coordinate the organized paracrystalline cargo
290 assembly of RuBisCO, with M58 limited to a peripheral sub-shell layer (Long *et al.,* 2007;
291 Cot *et al.,* 2008; Long *et al*., 2010; Long *et al*., 2011; Rae *et al*., 2013). Based on this
292 architecture, we expected M35 to assemble prior to M58 in the same manner as shell
293 recruitment follows RuBisCO (Chen *et al*., 2013). However, we were unable to resolve
294 any significant temporal difference between the CcmM isoforms. This concurrent timing
295 suggests that M58 interacts with RuBisCO even at the early stages of carboxysome
296 assembly, possibly in the internal core of the carboxysome. Assuming that the
297 carboxysome core grows by addition of material to the outside of a stable paracrystalline
298 RuBisCO assembly (Chen *et al*., 2013), these results also suggest that M58 does not
299 assemble as a separate layer around a pre-existing M35/RuBisCO core.
300
301 **M58 is not exclusive to a subshell layer**
302 3D-SIM experiments and quantitative analysis do not support a model of
303 carboxysome internal structure in which M58 is limited to a sub-shell localization. The
304 preexisting model described above proposes that M58 is not present within the primary
305 M35-Rubisco matrix. This makes logical sense based on the fact that M35, which does
306 not contain the N-terminal domain, presumably can achieve denser packing of RuBisCO
307 enzymes.
308 We expected that if M58 was in fact limited to a sub-shell layer ~5-6nm beneath
309 the outer surface, it would appear as a ring similar to CcmK4 by 3D-SIM. While SIM
310 imaging of CcmK4 did reveal the expected ring-like distribution, carboxysomes with

311 fluorescently-labeled M58 appeared predominantly as solid objects, with only a very a
312 small population (0.58%) showing dips in fluorescence intensity at their centers.
313 Consequently, we find no strong evidence by super-resolution microscopy to support a
314 model of carboxysome structure in which M58 is excluded from the carboxysome core,
315 suggesting that the internal carboxysome structure contains a mixed population of both
316 M35 and M58 coordinating with RuBisCO.

317 This finding raises new questions about the biogenesis of carboxysomes. For
318 example, M58 is thought to play a role in recruitment of shell components (Cot *et al*.,
319 2008; Long *et al.,* 2011; Kinney *et al*., 2012; Cameron *et al*., 2013). However, shell
320 proteins are recruited to carboxysomes only late in their maturation process (Chen *et al.,*
321 2013). Therefore, if M58 is present even at the early stages of carboxysome assembly,
322 what factors are responsible for delaying shell recruitment? This question is a promising
323 avenue for future work.

324

325 **Materials and Methods:**

326 **Western blot analysis**

327 For SDS-PAGE, log-phase ($OD_{750}$ = 1.0) cultures of cyanobacterial strains were
328 pelleted and frozen at -20°C. Frozen pellets were thawed in B-PER Bacterial Protein
329 Extraction Reagent (ThermoScientific), without DNAse or Lysozyme, and normalized by
330 wet pellet mass. Resuspended cells were mixed directly with SDS loading buffer and
331 boiled. Boiled samples were run on a 4-20% Tris-Glycine NuPAGE gel (Invitrogen) at
332 120V. SDS-PAGE separated proteins were transferred to a nitrocellulose membrane
333 with an iBlot2 transfer device (ThermoScientific).

334 The membrane was blocked with 5% skim milk in TBST (50mM Tris, 150mM
335 NaCl, 0.1% Tween 20), then probed with 1:10,000 of anti-CcmM primary antibody (a gift
336 of Ben Long), followed by a horseradish peroxidase-conjugated goat anti-rabbit

337 secondary antibody (Agrisera AS09 602). The membrane was incubated with
338 SuperSignal West Dura Extended Duration chemiluminescent substrate
339 (Thermoscientific) and imaged with the Bio-Rad ChemiDoc system.
340
341 **Transmission Electron Microscopy**
342 For TEM experiments, 1mL of mid-log cultures were pelleted (6k rpm, 5 min) and
343 concentrated 2x in sterile $dH_2O$. The cells were then mixed 1:1 with fixative (1.25%
344 formaldehyde, 2.5% glutaraldehyde, 0.03% picric acid, 0.1M sodium cacodylate buffer,
345 pH 7.4), incubated at RT for 30 min, then pelleted and stored in fixative at 4$^{o}$C overnight.
346 Fixed cells were embedded in epon resin and cut into ultra-thin sections (~60-80nm).
347 Sections were stained with uranyl acetate and lead citrate, then imaged on a Tecnai G2
348 Spirit Bio TWIN TEM.
349
350 **Cell culture**
351 Wild-type, mutant, and modified strains of *Synechococcus elongatus* PCC7942
352 were grown in BG-11 media, with 1 g/L HEPES adjusted to pH 8.5. Cultures were grown
353 at 30-35$^{o}$C under constant light with an approximate intensity of 1000 lm/m$^2$. Cultures
354 were grown in 125ml or 250ml flat bottom flasks, shaking at 150 rpm. Wild type 7942
355 and knockout complements were grown with ambient air conditions. Mutant
356 Δ*ccmM*::*HygR* cultures were supplemented with 2% $CO_2$ and 25 µg/mL hygromycin B.
357 Strains with fluorescently labeled carboxysome components, carrying kanamycin or
358 spectinomycin resistance genes, were grown with 25 µg/mL kanamycin or 25µg/mL
359 spectinomycin respectively. For the CcmM complement strain, Δ*ccmM* + *mTagBFP2-*
360 *CcmM-mNeonGreen*, cultures were grown with 5 µg/mL kanamycin and 25 µg/mL
361 hygromycin B. For growth curve experiments, biological replicates were made by
362 isolating colonies grown on BG11 agar with 1 g/L HEPES, 50mM $HCO_3^-$, and 1mM

363 $Na_2S_2O_3$. Isolates were screened by PCR to confirm the presence or absence of the WT
364 *ccmM* gene. Growth curve cultures were prepared by washing starter cultures in fresh
365 BG11 pH 8.5 media, then diluting to OD750 of ~0.1 in 40 mL BG11 in 250mL flat bottom
366 flasks.
367
368 **Image acquisition**
369 For both conventional fluorescence and 3D-SIM experiments, 5μL of either mid-
370 log cells ($OD_{750}$ = 1-2) for timelapse experiments or early-log cells ($OD_{750}$ = 0.5 - 1.2) for
371 3D-SIM were spotted on 2% agarose BG11 pads. Agarose pads were placed sample-
372 side down in MatTek 35mm glass bottom microwell dishes with No. 1.5 coverslips.
373 Sterile water was spotted within the dish to mitigate dehydration of the agarose pad, and
374 the dish was sealed with parafilm. Though strains expressing labeled CcmM were under
375 the control of the IPTG inducible promoter P*trc*, no induction was used with these cells
376 due to adequate basal expression. Cells expressing RbcL-sfGFP were imaged on BG11
377 agarose pads with the addition of 50μM IPTG following previously reported protocols
378 (Savage *et al*., 2010). SIM of uninduced RbcL-sfGFP cells also produced solid particles,
379 but were not as bright as induced cells and produced several false-positives in our
380 analysis pipeline (Supplemental figure S3). For timelapse experiments, samples were
381 recovered for >1h at 34-35°C, under ~1000 $lm/m^2$, and in ambient air, before being
382 imaged using a Nikon TE2000 and a 100x oil objective. Cells were kept at 30°C under
383 ~800 $lm/m^2$ light intensity during timelapse, and imaged every 10min.
384 3D-SIM data was collected on a DeltaVision OMX V4 Blaze system (GE
385 Healthcare) equipped with a 60x / 1.42 N.A. Plan Apo oil immersion objective lens
386 (Olympus), and three Edge 5.5 sCMOS cameras (PCO). mTagBFP2 fluorescence was
387 excited with a 405nm laser and collected with a 477/35 emission filter, mNeonGreen with
388 a 514nm laser and 541/22 emission filter, and sfGFP with a 488nm laser and a 528/48

389 emission filter. Z-stacks of ~2 microns were acquired with a z-step of 125 nm and with
390 15 raw images per plane (five phases, three angles). Spherical aberration was
391 minimized using immersion oil matching (Hiraoka *et al*., 1990). Super-resolution images
392 were computationally reconstructed from the raw datasets with a channel-specific
393 measured optical transfer function (OTF) and a Wiener filter constant of 0.001 using
394 CUDA-accelerated 3D-SIM reconstruction code based on Gustafsson *et al.*
395 *(*2008). Axial chromatic aberration was measured using TetraSpeck beads (Thermo
396 Fisher) a nano-grid control slide and multi-channel datasets were registered using the
397 image registration function in softWoRx.
398
399 **Image analysis**
400 SIM datasets were imported into MATLAB (Mathworks) using the bioformats
401 reader, followed by thresholding and background subtraction. The threshold value was
402 empirically determined and assessed by visualizing the resultant centroid position and
403 mask in MATLAB and Imaris (Bitplane AG) respectively. Segmented objects were further
404 analyzed if they met a cutoff for volume, surface area, sphericity, major-minor axis ratio,
405 and mean radius.
406 We calculated the MTC (max to center) ratio for each object. From the centroid,
407 the radially averaged intensity for each sub-sampled (0.5 pixels) radius was measured.
408 This was done for each Z-plane and then averaged over the Z-axis. A polynomial curve
409 was fit to the averaged radial profile of each segmented object in MATLAB. The most
410 suitable polynomial fit (up to 6th order) was selected based on meeting the Bayesian
411 Information Criterion. Then, the 1st and 2nd derivative of each fitted curve were
412 calculated to find the root with the global maximum. The intensity at this root was
413 calculated and divided by the intensity at the centroid. This ratio was calculated for each
414 object and plotted versus its mean radius in MATLAB.

415 Notably, the resolvable carboxysome ring limit of 220nm that we estimate in our
416 analysis is well above the ~110nm theoretical resolution limit of 3D-SIM (at 520nm
417 wavelength; Gustafsson *et al.,* 2000; Gustafsson *et al*., 2008). The difference is likely
418 due to a combination of practical limitations along with the probable overestimation of
419 carboxysome diameter in our analysis pipeline due to convolution of the true object size
420 with the point spread function in the fluorescence images.
421 Timelapse data of Δ*ccmM* + *mTagBFP2-CcmM-mNeonGreen* were processed
422 with ImageJ (FIJI) (Schindelin *et al*., 2012). Timelapse data from two sequential
423 acquisitions of the same field of view were imported into FIJI with the Bio-Formats Import
424 plugin with autoscaling, concatenated, and separated by channel. Channels were
425 registered using rigid registration in the StackReg FIJI plugin, then background
426 subtracted with a 50-pixel radius rolling ball. Particle tracking was performed in FIJI with
427 the TrackMate plugin using the LoG detector (Laplacian of Gaussian filter) with 0.5μm
428 estimated blob diameter, 0.5 threshold, and sub-pixel localization. Automatically
429 generated tracks were manually extended backwards in time 20-30 frames by selecting
430 0.5μm diameter regions at or near site where the particle was first detected in order to
431 capture a background fluorescence level. Particle tracks were corrected for
432 photobleaching by dividing intensities by an average of 7 reference particles, normalized
433 to the first frame of the time lapse, in each channel. Reference particles were objects
434 observed to be relatively stable compared to particles that lost or gained fluorescence
435 due to carboxysome biogenesis. The same reference particles were used for correction
436 in both channels. To generate the timelapse montage, brightness and contrast values
437 were manually adjusted separately in each channel to enhance visibility in the figure.
438
439 **Cloning and strain construction**

440 Plasmids used for *S. elongatus* strain construction were made by Gibson
441 assembly. Tagged CcmM plasmids were cloned by inserting the *ccmM* gene, along with
442 mNeonGreen and mTagBFP2 coding sequences with additional flexible linker
443 sequences, into the previously described pDFS21 neutral site II (NS2) integration
444 plasmid downstream of the IPTG inducible P*trc* promoter (Savage *et al*., 2010). The
445 *ccmM* gene was obtained directly from the *S. elongatus* PCC7942 genome via PCR with
446 Phusion polymerase (NEB). The *ccmK4* gene for cloning shell fusion plasmids was
447 obtained as a synthesized gBlock (IDT) and cloned into the pDFS21 integration plasmid.
448 *S. elongatus* strains were transformed with integration plasmids by incubating ~5
449 fold concentrated $OD_{750}$ 1-2 culture with 10-100ng plasmid at 30$^{o}$C in the dark overnight,
450 followed by plating transformants on selective BG11 agar (Clerico *et al*., 2007). The
451 mutant Δ*ccmM* strain was made by integrating a hygromycin B resistance gene into the
452 native *ccmM* ORF, followed by selective plating and screening (Sachdeva G., 2014).
453

454 **Acknowledgements**

455 We thank Ben Long (ANU) for many helpful discussions and the kind gift of anti-
456 CcmM serum, Jennifer Waters and the Harvard Cell Biology Microscopy Facility for their
457 guidance on SIM acquisition and analysis, Lin Shao for CUDA-accelerated SIM
458 reconstruction code, Hunter Elliott (Harvard Medical School) for his great help and
459 intellectual input on developing the SIM analysis pipeline, David Savage (UC Berkeley)
460 for collaborating with us on exploring other microscopy methods, the Harvard Medical
461 School EM facility for all their amazing work preparing samples and helping us with EM
462 imaging. We would also like to acknowledge Gairik Sachdeva and Simon Kretschmer
463 who originally constructed the Δ*ccmM::HygB* knockout strain in the Silver lab.
464

465 **References**

Andersson I, Backlund A. (2008). Structure and function of Rubisco. Plant Physio and Biochem. 46:275-291.

Badger MR, Hanson D, Price GD. (2002). Evolution and diversity of CO2 concentrating mechanisms in cyanobacteria. Funct. Plant Biol. 29:161–173.

Badger MR, Price GD. (2003). CO2 concentrating mechanisms in cyanobacteria: molecular components, their diversity and evolution. J Exp. Bot. 54:609–622.

Ball G, Demmerle J, Kaufmann R, Davis I, Dobbie IM, Schermelleh L. (2015). SIMcheck: a Toolbox for Successful Super-resolution Structured Illumination Microscopy. Sci Rep. 5:15915.

Berla BM, Saha R, Immethun CM, Maranas CD, Moon TS, Pakrasi HB. (2013). Synthetic biology of cyanobacteria: unique challenges and opportunities. Front Microbiol. 4(246):1-14.

Cameron JC, Wilson SC, Bernstein SL, Kerfeld CA. (2013). Biogenesis of a bacterial organelle: the carboxysome assembly pathway. Cell. 155:1131-1140.

Chen AH, Robinson-Mosher A, Savage DF, Silver PA. Polka JK. (2013). The bacterial carbon-fixing organelle is formed by shell envelopment of preassembled cargo. PLOS One. 8(9):1-13.

Clerico EM, Ditty JL, Golden SS. (2007). Specialized techniques for site-directed mutagenesis in cyanobacteria. Methods Mol Biol. 362:155-171.

Cot SS, So AK, Espie GS. (2008). A multiprotein bicarbonate dehydration complex essential to carboxysome function in cyanobacteria. J Bacteriol. 190:936-945.

Gustafsson MGL. (2000). Surpassing the lateral resolution limit by a factor of two using structured illumination microscopy. J of Microsc. 198(2):82-87.

Gustafsson MGL, Shao L, Carlton PM, Wang CJR, Golubovskaya IN, Cande WZ, Agard DA, Sedat JW. (2008). Three-dimensional resolution doubling in wide-field fluorescence microscopy by structured illumination. Biophys J. 94:4957-4970.

Hiraoka Y, Sedat JW, Agard DA. (1990). Determination of three-dimensional imaging properties of a light microscope system. Partial confocal behavior in epifluorescence microscopy. Biophys J. 57(2):325-333.

Kaneko Y, Danev R, Nagayama K, Nakamoto H. (2006). Intact carboxysomes in cyanobacterial cell visualized by Hilbert Differential Contrast Transmission Electron Microscopy. J Bacteriol. 188(2):805-808.

Kerfeld CA, Melnicki MR. (2016). Assembly, function and evolution of cyanobacterial carboxysomes. 32:66-75.

Kinney JN, Salmeen A, Cai F, Kerfeld CA. (2012). Elucidating essential role of conserved carboxysomal protein CcmN reveals common feature of bacterial microcompartment assembly. 2012. J Biol Chem. 287(21):17729-17736.

Long BM, Murray BR, Whitney SM, Price GD. (2007). Analysis of carboxysomes from *Synechococcus* PCC7942 reveals multiple rubisco Complexes with carboxysomal proteins CcmM and CcaA. J Biol Chem. 282(40):29323-29335.

Long BM, Rae BD, Badger MR, Price GD. (2011). Over-expression of the ß-carboxysomal CcmM protein in *Synechococcus* PCC7942 reveals a tight co-regulation of carboxysomal carbonic anhydrase (CcaA) and M58 content. Photosynth Res. 109:33-45.

Long BM, Tucker L, Badger MR, Price GD. (2010). Functional cyanobacterial ß-carboxysomes have an absolute requirement for both long and short forms of the CcmM Protein. Plant Physiol. 153:285-293.

Polka JK, Silver PA. (2013). Building synthetic cellular organization. Mol Biol Cell. 24:3585-3587

Price GD, Howitt SM, Harrison K, Badger MR. (1993). Analysis of a genomic DNA region from the cyanobacterium *Synechococcus* sp. Strain PCC7942 involved in carboxysome assembly and function. J Bacteriol. 175(10):2871-2879.

Price GD, Badger MR, Woodger FJ, Long BM. (2007). Advances in understanding the cyanobacterial $CO_2$-concentrating-mechanism (CCM): functional components, Ci transporters, diversity, genetic regulation and prospects for engineering into plants. J Exper Bot. 59(7):1441-1461.

Rae BD, Long BM, Badger MR, Price GD. (2012). Structural determinants of the outershell of ß-carboxysomes in *Synechococcus elongatus* PCC7942: roles for CcmK2, K3-K4, CcmO, and CcmL. PLOS One. 7(8):1-11.

Rae BD, Long BM, Badger MR, Price GD. (2013). Functions, compositions, and evolutions of the two types of carboxysomes: polyhedral microcompartments that facilitate $CO_2$ fixation in cyanobacteria and some proteobacteria. Microbiol Mol Biol Rev. 77(3):357-379.

Rae BD, Long BM, Whitehead LF, Förster B, Badger MR, Price GD. (2013). Cyanobacterial carboxysomes: microcompartments that facilitate $CO_2$ fixation. J Mol Microbiol Biotechnol. 23:300-307.

Sachdeva G. (2014). Controlling fluxes for microbial metabolic engineering. Doctoral dissertation, Harvard University.

Savage DF, Afonso B, Chen AH, Silver PA. (2010). Spatially ordered dynamics of the bacterial carbon fixation machinery. Science. 327:1258-1261.

Schindelin J, Arganda-Carreras I, Frise E. *et al*. (2012). Fiji: an open-source platform for biological-image analysis. Nature Methods. 9(7): 676-682.

Schindelin J, Rueden CT, Hiner MC, Eliceiri KW. (2015). The ImageJ ecosystem: An open platform for biomedical image analysis. Mol Reprod Dev. 82(7-8):518-29.

Tanaka S, Sawaya M, Philips M, Yeates T. (2008). Insights from multiple structures of the shell proteins from the ß-carboxysome. Prot Sci. 18:108-120.

Woodger FJ, Badger MR, Price GD. (2005). Sensing of inorganic carbon limitation in *Synechococcus* PCC7942 is correlated with the size of the internal inorganic carbon pool and involves oxygen. Plant Physiol. 139(4):1959-1969.

Yokoo R, Hood RD, Savage DF. (2015). Live-cell imaging of cyanobacteria. Photosynth Res. 126(1):33-46.

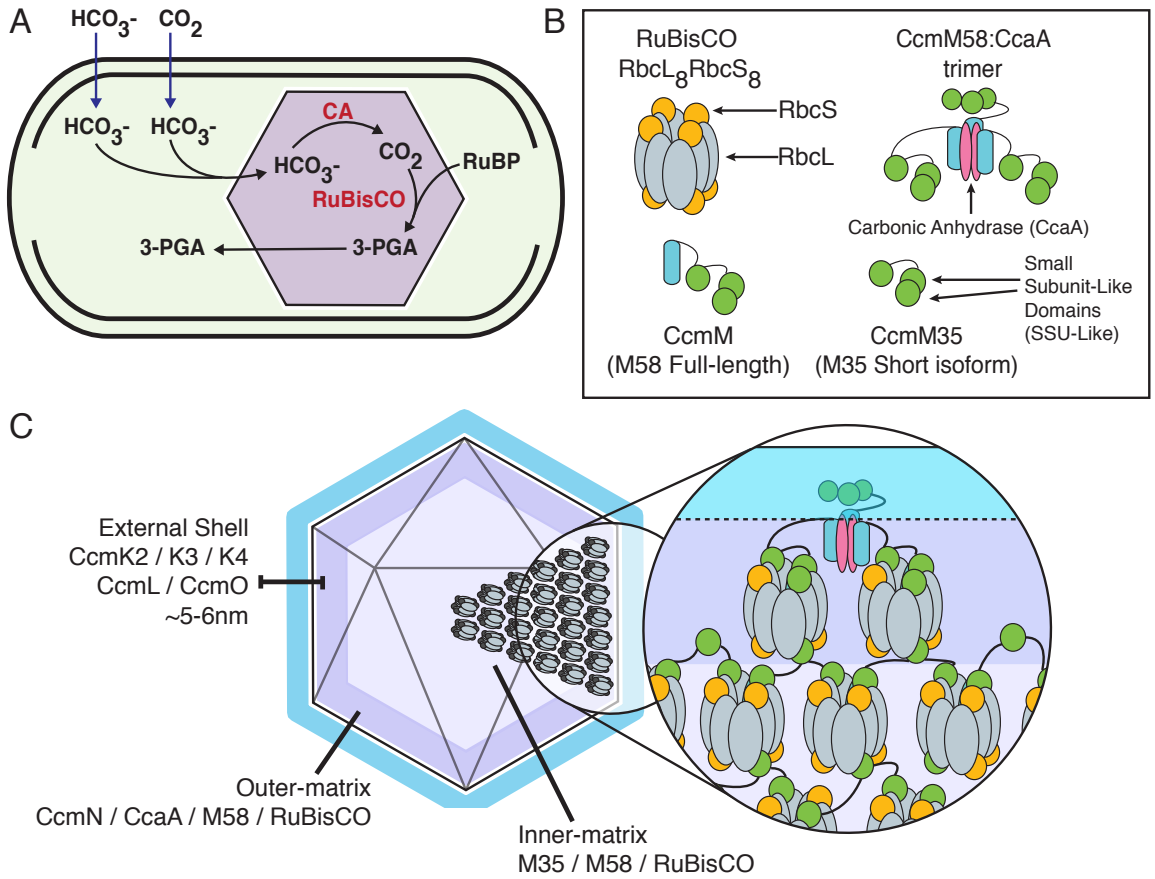


Figure 1. Current model of the cyanobacterial carboxysome internal structure. (A) *S. elongatus* utilizes the carboxysome to concentrate and protect its RuBisCO enzymes. Through a multi-step process, bicarbonate passes into the carboxysome, is converted to $CO_2$ by carbonic anhydrase, and is then fixed by RuBisCO to form 3-phosphoglyceric acid (3-PGA). (B) Legend of proteins and protein complexes of the carboxysomes interior. *CcmM* is an essential carboxysome gene that is translated as two different isoforms, the full-length 58kDa M58 and a truncated 35kDa form, M35. CcmM has an N-terminal domain that complexes with CcaA carbonic anhydrase, and three repetitive C-terminal domains that have homology with the small subunit of RuBisCO. (C) These small subunit-like domains (SSU-like), which make up the majority of the M35 protein, are believed to displace a portion of the RuBisCO small subunits and physically tether the enzymes together within the core of the carboxysome, to the exclusion of the long M58 isoform which has been hypothesized to remain just beneath the carboxysome shell.

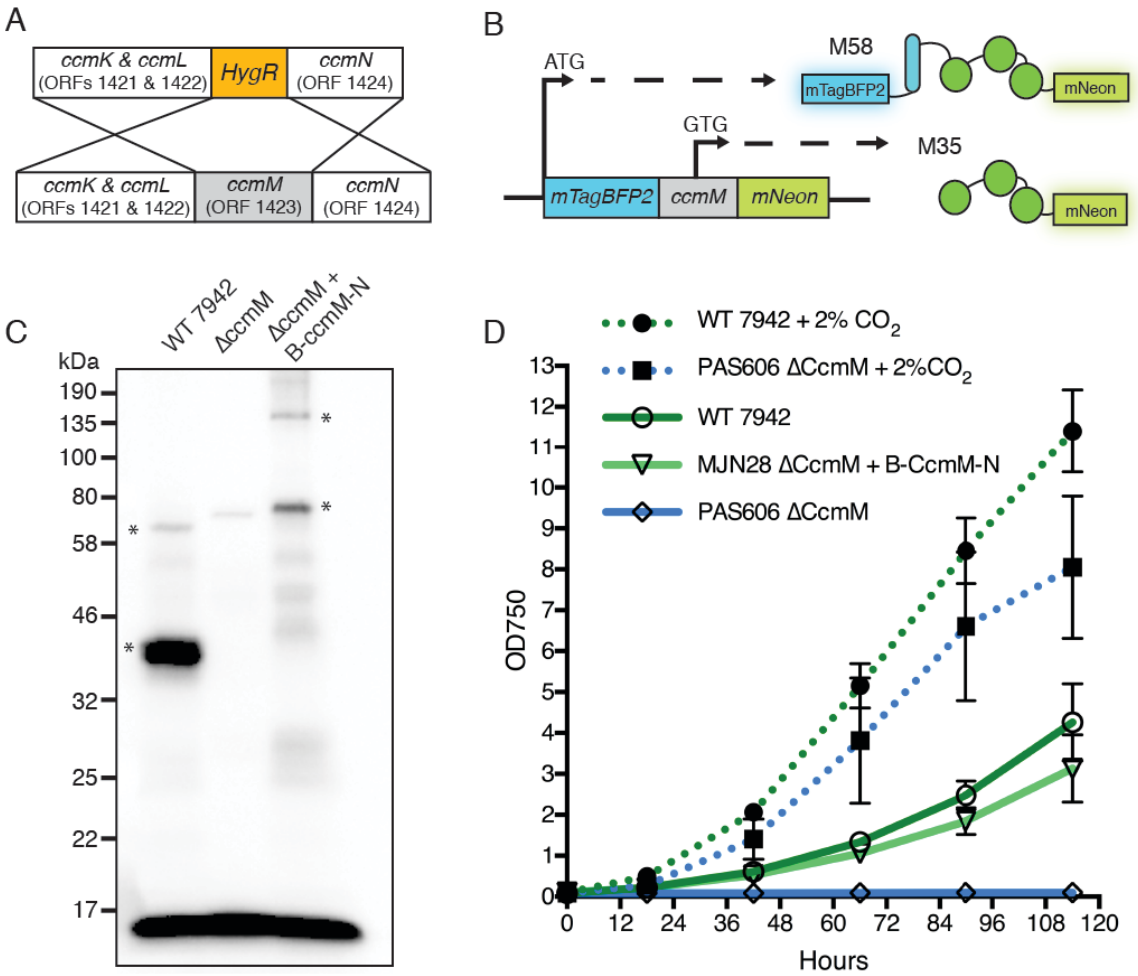


Figure 2. Fluorescently tagged *ccmM* integrated into the genome of a Δ*ccmM* knockout produces both CcmM isoforms and and restores growth in ambient air conditions. (A) The Δ*ccmM* knockout was made by integrating a hygromycin resistance marker into the genomic site of *ccmM*. (B) Diagram of fluorescently tagged *ccmM*. N- and C-terminal fusions of mTagBFP2 and mNeonGreen produces short and long isoforms with different fluorescent characteristics. This construct was integrated at Neutral Site II of the 7942 Δ*ccmM* genome to yield the Δ*ccmM* + *mTagBFP2-CcmM-mNeonGreen (+B-ccmM-N)* strain. (C) Anti-CcmM western blot of WT, Δ*ccmM*, and *+B-ccmM-N*. Full length M58 isoform of CcmM is ~58 kDa, while the truncated M35 is ~35 kDa. The fluorescent fusions of mTagBFP2-M58-mNeonGreen and M35-mNeonGreen have expected molecular weights of approximately 113 kDa and 63 kDa respectively. (D) Growth curves of WT 7942, Δ*ccmM*, and the *+B-ccmM-N* genetic complement. Dotted lines denote cultures grown with 2% supplemented $CO_2$. Solid lines denote cultures grown in ambient air conditions. n = 3 biological replicates, error bars = standard deviation.

Figure 3. Transmission electron micrographs show the formation of carboxysomes in Δ*ccmM* cells complemented with fluorescently tagged *ccmM*. (A-D) Carboxysomes (white arrows) in wild type PCC7942 cells show characteristic hexagonal geometry. Diameters of WT carboxysomes labeled in micrographs range from 150 - 280 nm with an average of 180 ± 33nm (N=???). (E-H) Micrographs of the Δ*ccmM* knockout show the absence of carboxysomes. (I-L) Integration of the fluorescently tagged *ccmM* construct *B-ccmM-N* into the Δ*ccmM* knock out rescues the formation of apparently normal carboxysomes. These carboxysomes had geometry similar to that observed in wild type cells. Carboxysomes with tagged CcmM appeared to range more widely in size than in wild type cells with an average diameter of 319 ± 92nm (N=???). Some (J & L) were of typical size (200nm in diameter), while others (K) are larger at 300-330 nm. Larger carboxysomes were also observed, like that seen in (I), which approaches 600nm at its widest point.

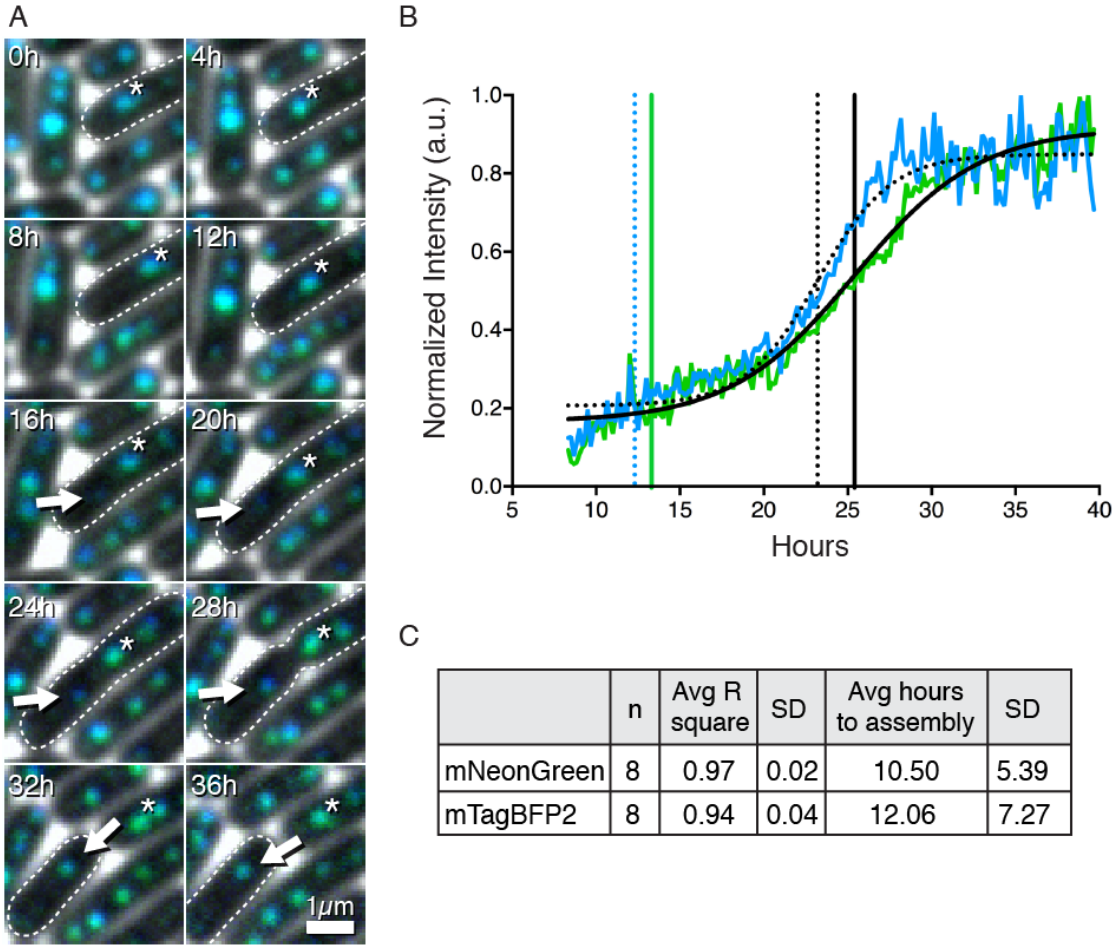


C

| | n | Avg R square | SD | Avg hours to assembly | SD |
|---|---|---|---|---|---|
| mNeonGreen | 8 | 0.97 | 0.02 | 10.50 | 5.39 |
| mTagBFP2 | 8 | 0.94 | 0.04 | 12.06 | 7.27 |

Figure 4. CcmM isoforms co-assemble at the site of new carboxysomes. (A) Merged montage of carboxysome biogenesis in the Δ*ccmM* + *mTagBFP2-ccmM-mNeonGreen* gene complement strain shows simultaneous co-localization of both blue (mTagBFP2-M58) and green (M58-mNeonGreen / M35-mNeonGreen) particles. White arrows indicate the new carboxysome. White asterisk indicates the parent carboxysome. (B) Channel specific intensity plots of carboxysome biogenesis depicted in panel A reveal sigmoidal-like dynamics in assembly timing in M35 and M58 CcmM isoforms. Vertical blue and green lines denote point at which automatic particle tracking first identified the new carboxysome. Tracks were extended backwards to measure background by manually measuring spot at or near the new particle (Methods). Four-parameter logistic equations were fit to each track; black solid or dotted vertical lines denote half-max values of each channel. (C) Statistics of sigmoidal curves fit to 8 measured biogenesis events find similar assembly dynamics in both green and blue channels. Assembly time was measured from first time point of automatic tracking to first value $\geq$ 0.8 on normalized intensity plot.

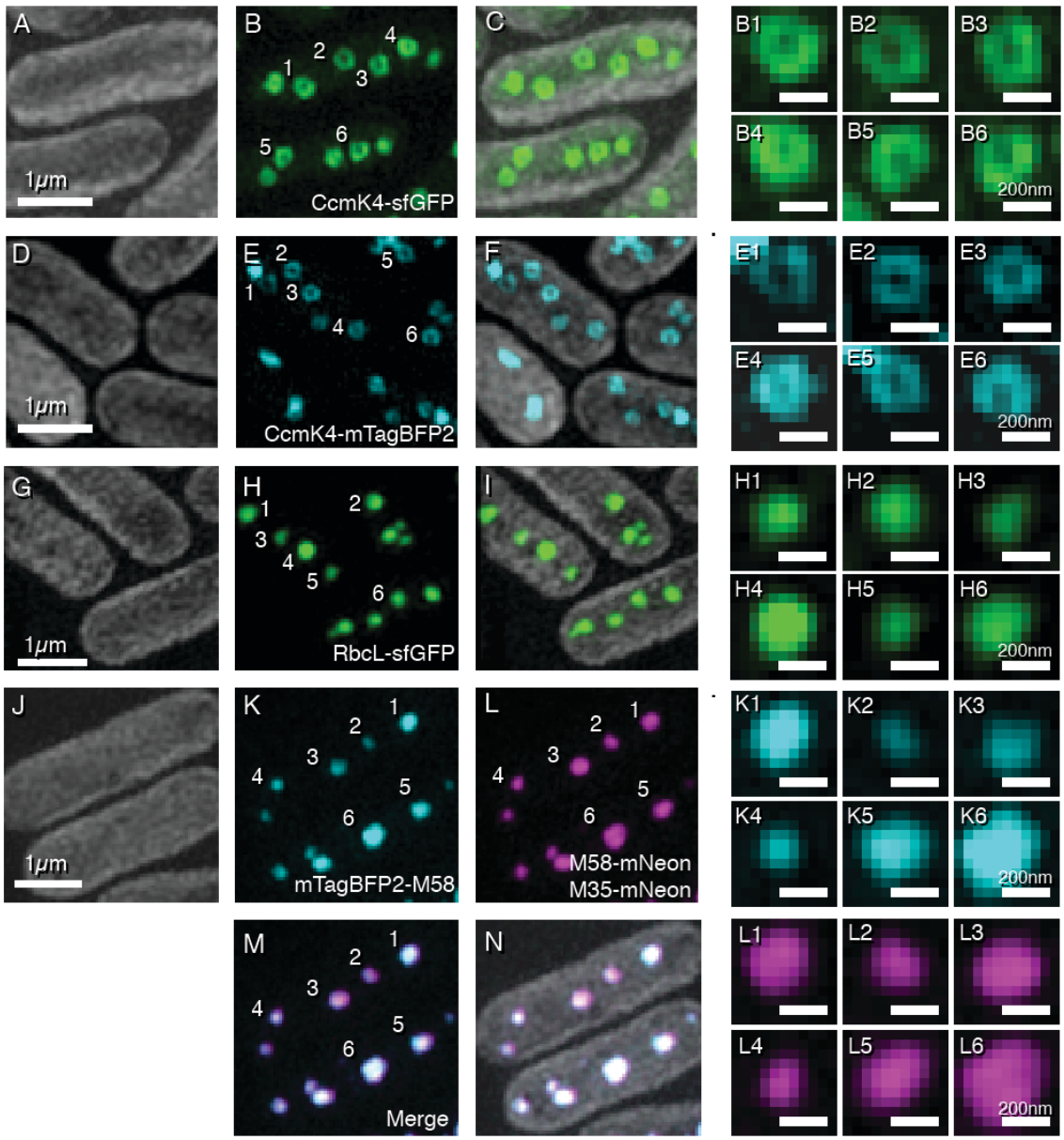


Figure 5. SIM of fluorescently tagged carboxysomes resolves the ring of the outer shell, and an absence of shell-like localization of either RuBisCO or CcmM. (A-C) SIM of CcmK4-mTagBFP2 resolves the carboxysome shell as a hollow ring, while (D-F) SIM of RbcL-sfGFP produces solid particles. (G-K) SIM of Δ*ccmM* + *mTagBFP2-ccmM-mNeonGreen* produces RuBisCO-like, apparently solid particles. M35/M58-mNeonGreen particles are pseudocolored magenta. Numbers identify individual carboxysomes and correspond to magnified panels on the right.

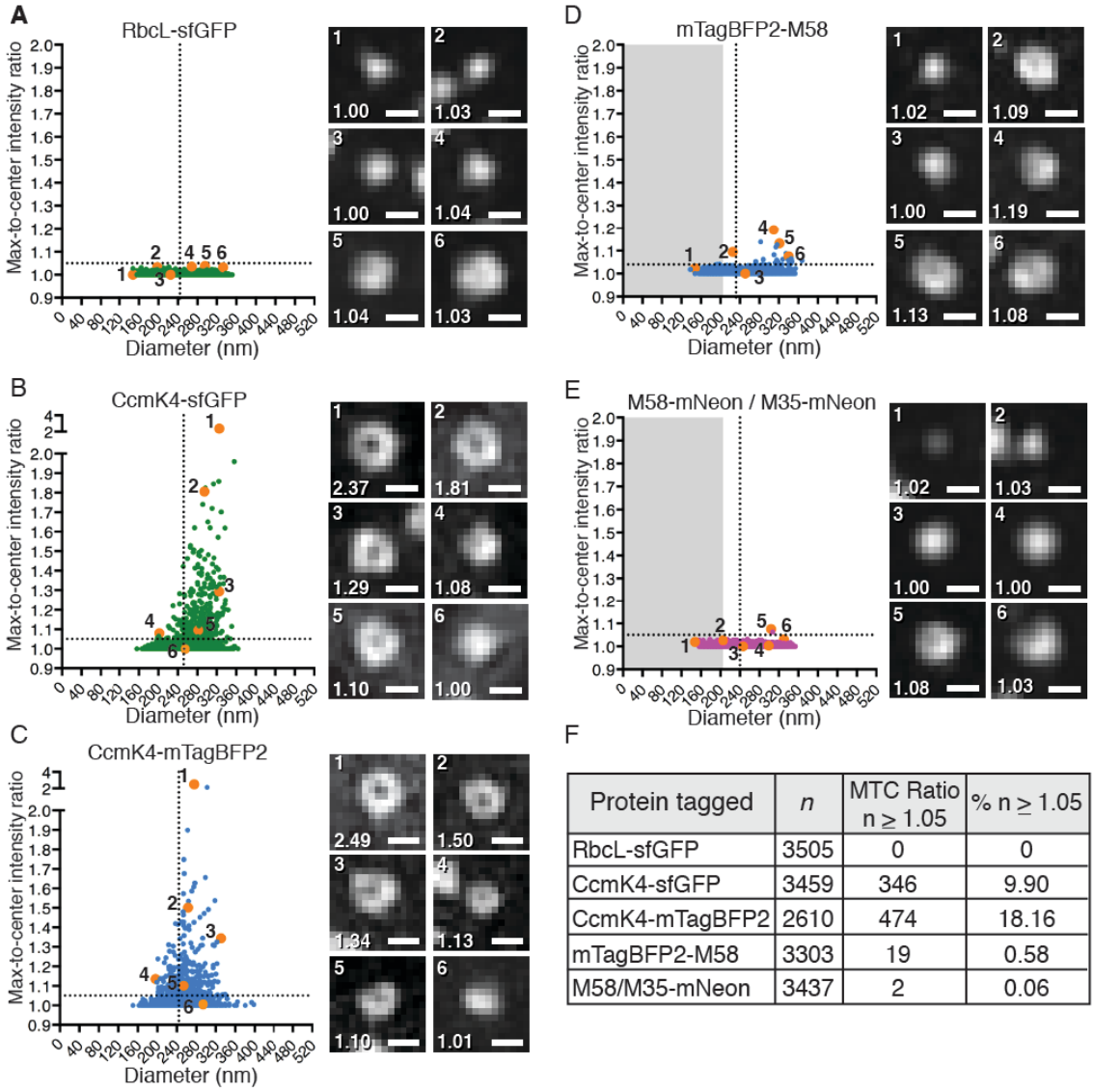


| Protein tagged | *n* | MTC Ratio n ≥ 1.05 | % n ≥ 1.05 |
|---|---|---|---|
| RbcL-sfGFP | 3505 | 0 | 0 |
| CcmK4-sfGFP | 3459 | 346 | 9.90 |
| CcmK4-mTagBFP2 | 2610 | 474 | 18.16 |
| mTagBFP2-M58 | 3303 | 19 | 0.58 |
| M58/M35-mNeon | 3437 | 2 | 0.06 |

Figure 6. Analysis of 3D-SIM data. Using radially averaged intensity profiles of fluorescent particles in 3D-SIM data, maximum intensity to center (MTC) intensity ratios can measure the degree to which a fluorescent object is resolved as a ring. (A) Analysis of RbcL-sfGFP 3D-SIM data found no objects with a max-to-center ratio (MTC) greater than 1.04, with an average ratio of 1.002 ± 0.005 and average particle size of 244 ± 45 nm marked by the vertical line. An upper ratio limit of 1.05, below which objects are likely to be solid, was calculated by adding two standard deviations to the RbcL-sfGFP max ratio. The 1.05 MTC cutoff is marked by a horizontal line on all plots. (B) Size versus intensity ratio plot of CcmK4-sfGFP shows a population of particles (345, 9.97%) with MTC ratios ≥ 1.05. (C) Plot of CcmK4-mTagBFP2 shows a two-fold increase in the fraction of ring-like particles compared to the GFP tagged version (474, 18.16%). (D) Analysis of particles in the blue channel of the Δ*ccmM* ± *mTagBFP2-CcmM-mNeonGreen* strain, representing M58, finds only a few particles with noticeable ring-like appearance (19, 0.58%), with the vast majority of particles appearing

solid. Based on the size of smallest detected ring in the tagged shell strains (196nm) and a shell thickness of 5-6nm, the minimum diameter at which ring-like shapes can be detected is calculated as 220nm; this is marked in gray. Ring-like particles within this region are unlikely to be resolved due to their small size. (E) Plot of particles in the green channel of Δ*ccmM* + *mTagBFP2-CcmM-mNeonGreen* strain, representing M58-mNeonGreen and M35-mNeonGreen are predominantly solid with only 2 ring-like structures identified (2, 0.06%). (F) Table summarizing analysis statistics. In microscopy panels, scale bars are 200nm, and numbers denote MTC ratio.

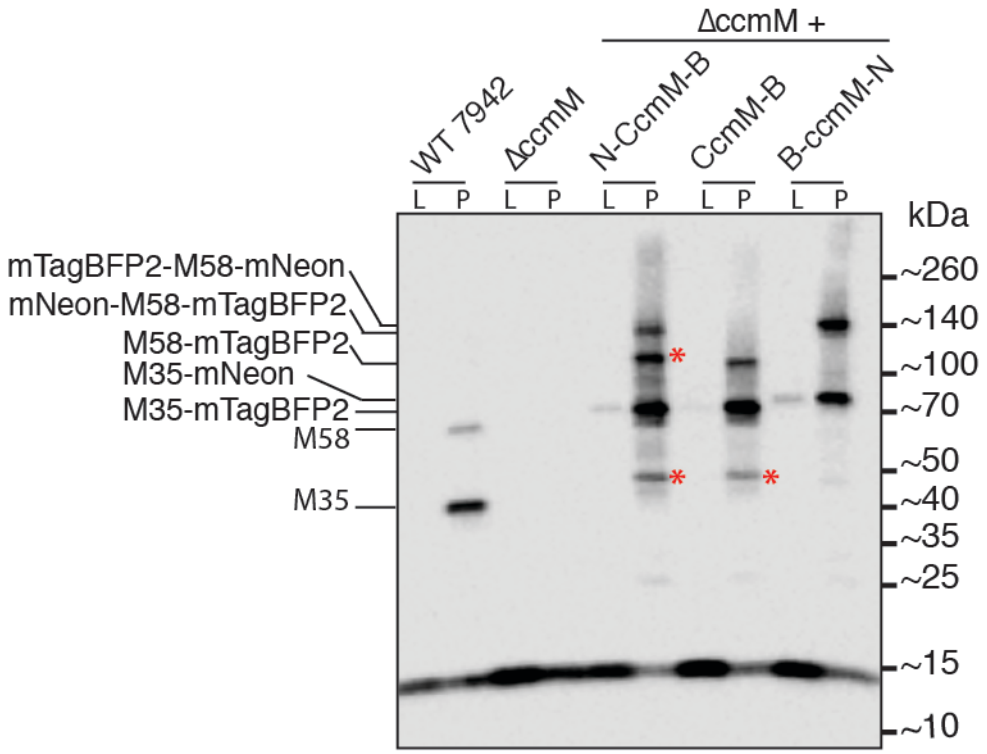


Figure S1. Protein degradation in variant *ccmM* gene complements. Western blot analysis of Δ*ccmM* + *mNeonGreen-ccmM-mTagBFP2*, and Δ*ccmM* + *ccmM-mTagBFP2* revealed prominent unexpected bands (marked by red asterix) that could be indicative of protein degradation in the cell. The Δ*ccmM* + *mTagBFP2-ccmM-mNeonGreen* strain did not show similar unexpected bands. L = cell lysate and P = post-lysis pellet.

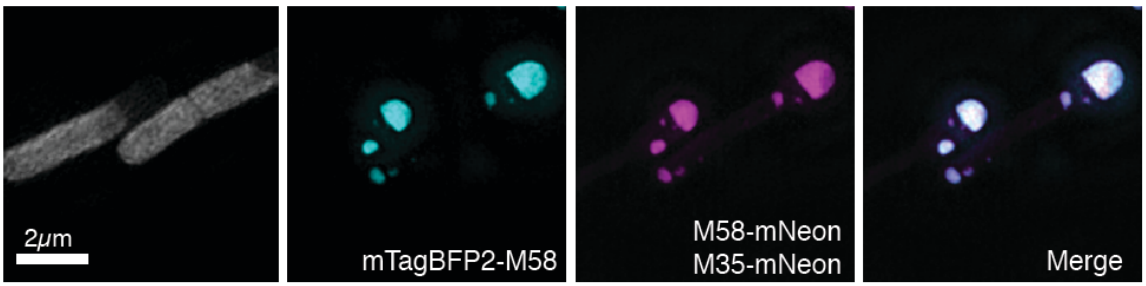


Figure S2. Induction of the P*trc*::Δ*ccmM* + *mTagBFP2-ccmM-mNeonGreen* in *S. elongatus* leads to protein aggregation**.** SIM images of Δ*ccmM* + *mTagBFP2-ccmM-mNeonGreen* cells induced with 50μM IPTG show large aggregations of fluorescent signal near the cell polls.

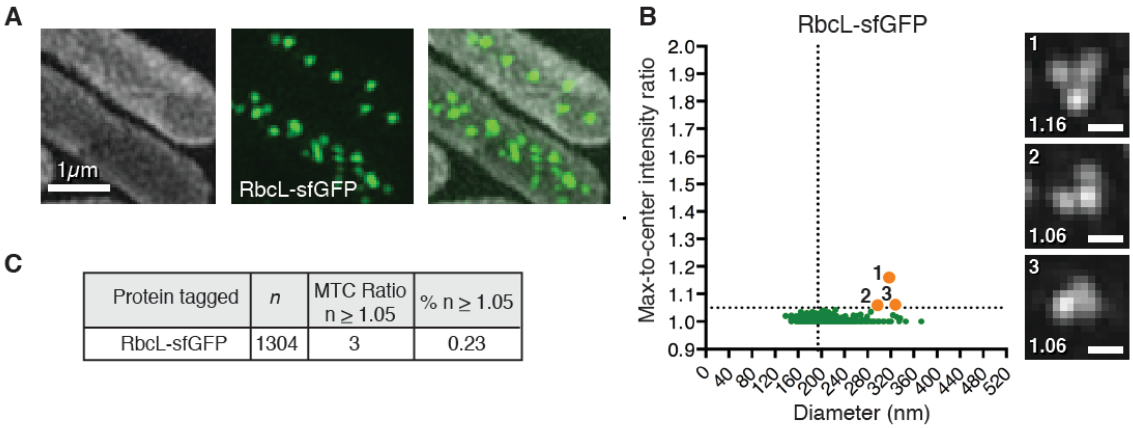


| Protein tagged | *n* | MTC Ratio n ≥ 1.05 | % n ≥ 1.05 |
|---|---|---|---|
| RbcL-sfGFP | 1304 | 3 | 0.23 |

Figure S3. Uninduced cells expressing RbcL-sfGFP still produce solid particles. Qualitative data and image analysis results of PCC7942 RbcL-sfGFP cells without any IPTG induction show similar incidence of low MTC ratio solid particles compared to cells induced with 50μM IPTG. Three particles were identified as ring-like with MTC ratios > 1.05, but were confirmed to be three particle clusters incorrectly analyzed as single objects by our analysis program.

| Strain | Tag | IPTG (μM) | # Imgs | Refractive Index | Wiener Filter | RIH (477) | RIH (528) | RIH (541) | RIH (608) |
|---|---|---|---|---|---|---|---|---|---|
| DFS724 | RbcL-sfGFP | 50 | 31 | 1.518 | 0.01 | | 12.74 ± 1.63 | | 2.78 ± 0.66 |
| AHC134 | CcmK4-sfGFP | - | 31 | 1.517 | 0.01 | | 13.15 ± 1.78 | | 3.53 ± 1.08 |
| MJN31 | CcmK4-mTagBFP2 | 0 | 29 | 1.517 | 0.01 | 8.28 ± 1.84 | | | 2.77 ± 0.96 |
| MJN28 | mTagBFP2-CcmM-mNeon | 0 | 47 | 1.517 | 0.01 | 9.45 ± 2.80 | | 12.58 ± 2.51 | 3.10 ± 0.84 |

Tables S1. Structured Illumination Microscopy reconstruction scores. Reconstructed Intensity Histogram scores (RIH) were averaged across all image sets for each strain used for image analysis. Scores of 6-12 are considered good, and greater than 12 excellent. Columns with RIH scores are channel specific. Channel 608 captured the red auto-fluorescence of cells which was not used for any analysis. Error = Standard deviation.

**A**

| Welch's ANOVA | Degrees of freedom | $F_s$ | *P* |
|---|---|---|---|
| Among groups | 4.00 | 160.48 | 6.51 x 10-132 |
| Within groups | 7377.44 | | |

**B**

| Games-Howell test | Mean difference | q | > $q_{crit}$ 5.484 (α=0.001) |
|---|---|---|---|
| CcmM-mNeon vs CcmK4-sfGFP | 0.020465 | 22.20 | Significant |
| CcmM-mNeon vs CcmK4-mTagBFP2 | 0.033914 | 26.34 | Significant |
| CcmM-mNeon vs mTagBFP2-CcmM | 0.001283 | 9.56 | Significant |
| CcmM-mNeon vs RbcL-sfGFP | 0.000050 | 0.57 | Not significant |
| CcmK4-sfGFP vs CcmK4-mTagBFP2 | 0.013449 | 8.51 | Significant |
| CcmK4-sfGFP vs mTagBFP2-CcmM | 0.019182 | 20.69 | Significant |
| CcmK4-sfGFP vs RbcL-sfGFP | 0.020515 | 22.26 | Significant |
| CcmK4-mTagBFP2 vs mTagBFP2-Ccm | 0.032631 | 25.27 | Significant |
| CcmK4-mTagBFP2 vs RbcL-sfGFP | 0.033964 | 26.38 | Significant |
| mTagBFP2-CcmM vs RbcL-sfGFP | 0.001333 | 10.05 | Significant |

Table S2. Statistical test results of particle MTC ratio comparison.

| Strain or Plasmid | Genotype | Resistance | Reference |
|---|---|---|---|
| *E-coli strains* | | | |
| DH5-alpha | Host strain for plasmid construction (PAS644) | | |
| DH10-beta | Host strain for plasmid construction (PAS641, PAS642, PAS643) | | |
| Turbo | Host strain for plasmid construction (PAS645) | | |
| *S. elongatus strains* | | | |
| PCC7942 | Wild-type *Synechococcus elongatus,* ATCC 33912 | | |
| Δ*ccmM* | PCC7942 Δ*ccmM*::*HygR* knock out | HygB | |
| PAS646 | PCC7942 *Ptrc:CcmK4-mNeon* integrated in NS2 | Kan | This work |
| PAS647 | PCC7942 Δ*CcmM::HygR + Ptrc:mNeon-CcmM-mTagBFP2* integrated in NS2 | HygB, Kan | This work |
| PAS648 | PCC7942 Δ*CcmM::HygR + Ptrc:CcmM-mTagBFP2* integrated in NS2 | HygB, Kan | This work |
| PAS649 | PCC7942 Δ*CcmM::HygR + Ptrc:mTagBFP2-CcmM-mNeon* integrated in NS2 | HygB, Kan | This work |
| PAS650 | PCC7942 *Ptrc:CcmK4-mTagBFP2* integrated in NS2 | Kan | This work |
| PAS651 | PCC7942 *Papca:CcmK4-mNeon* integrated in NS1 | Sp | Chen et al., 2013 |
| PAS652 | PCC7942 *Ptrc:RbcL-sfGFP* integrated in NS2 | Kan | Savage et al., 2010 |
| *Plasmids* | | | |
| pAM2314 | *S. elongatus* Neutral Site I integration vector | Sp | Mackey et al., 2007 |
| pAM1579 | *S. elongatus* Neutral Site II integration vector | Kan | Mackey et al., 2007 |
| pDFS21 | derivative of pAM1579 with *trc* promoter from pTRC99 and *lacI* | Kan | Savage et al., 2010 |
| pAHC134 | P*apca*::*ccmK4-sfGFP* | Sp | Chen et al., 2013 |
| pDFS724 | P*trc*::*RbcL-sfGFP* | Kan | Savage et al., 2010 |
| PAS641 | P*trc::mNeonGreen-CcmM-mTagBFP2* cloned into pDFS21 at XbaI and NotI sites | Kan | This work |
| PAS642 | P*trc::CcmM-mTagBFP2* cloned into pDFS21 at XbaI and NotI sites | Kan | This work |
| PAS643 | P*trc::mTagBFP2-CcmM-mNeonGreen* cloned into pDFS21 at XbaI and NotI sites | Kan | This work |
| PAS644 | *Ptrc::CcmK4-mNeonGreen* cloned into pDFS21 at XbaI and NotI sites | Kan | This work |
| PAS645 | *Ptrc::CcmK4-mTagBFP2, mTagBFP2* cloned in place of *mNeonGreen* in pDFS21 | Kan | This work |

Table S3. Strains and plasmids